Article

Not peer-reviewed version

Preparation of a Nano-laminated Sc2SnC MAX Phase Coating on SiC Fibers via the Molten Salt Method

Chenyang Wang , Lexiang Yin , Peng Li * , Qing Huang *

Posted Date: 29 May 2025

doi: 10.20944/preprints202505.2322.v1

Keywords: MAX phase coating; Molten salt synthesis; SiC fiber; Pyrolytic carbon; CVD

 doi:10.20944/preprints202505.2322.v1

Article

Preparation of a Nano-laminated Sc_2SnC MAX Phase Coating on SiC Fibers via the Molten Salt Method

Chenyang Wang [1,2], Lexiang Yin [2], Peng Li [2,*] and Qing Huang [2,*]

[1] School of Materials Science and Chemical Engineering, Ningbo University, Ningbo 315211, China

[2] Zhejiang Key Laboratory of Data-Driven High-Safety Energy Materials and Applications, Ningbo Key Laboratory of Special Energy Materials and Chemistry, Advanced Nuclear Materials Laboratory, Ningbo Institute of Materials Technology and Engineering, Chinese Academy of Sciences, Ningbo 315201, China

* Correspondence: lipeng@nimte.ac.cn (P.L.); huangqing@nimte.ac.cn (Q.H.)

Abstract: The incorporation of MAX phase interface layers into silicon carbide (SiC) composites has been shown to significantly enhance mechanical properties, particularly under irradiation conditions. However, conventional Ti-based MAX phases suffer from thermal instability and tend to decompose at high temperatures. In this work, Sc_2SnC coating was successfully synthesized on the surface of SiC fibers (SiC_f) via an in-situ reaction between metals and pyrolytic carbon (PyC) in a molten salt environment. The PyC layer, pre-deposited by chemical vapor deposition (CVD), served as both a carbon source and a structural template. Characterization by SEM, XRD, and Raman spectroscopy confirmed the formation of Sc_2SnC coatings with a distinctive hexagonal flake-like morphology, accompanied by an internal ScC_x intermediate layer. By turning the Sc-to-Sn ratio in the molten salt, coatings with varied morphologies were achieved. ScC_x was identified as a critical intermediate phase in the synthesis process. The formation of numerous defects during the reaction enhanced element diffusion, resulting in preferential growth orientations and diverse grain structures in the Sc_2SnC coating.

Keywords: MAX phase coating; Molten salt synthesis; SiC fiber; Pyrolytic carbon; CVD

1. Introduction

Silicon carbide (SiC) based ceramics and their composites (SiC_f/SiC) are regarded as promising materials for components in light water reactor (LWR) and advanced fission reactors, including high-temperature gas-cooled reactors (HTGRs), fluoride-salt-cooled high-temperature reactors (FHRs), and gas-cooled fast reactors (GFRs) [1]. The interfacial layer between SiC fibers (SiC_f) and the SiC matrix plays a crucial role in integrating the mechanical, thermal, and electrical properties of the fibers and the matrix. This layer can significantly improve the composite's strength, fracture toughness, resistance to radiation, oxidation, and corrosion, as well as thermal conductivity. However, under nuclear irradiation conditions, it is necessary to develop an interface layer that can withstand high temperatures and radiation, because conventional interfacial layers are prone to structural degradation and performance failure [2]. For example, pyrolytic carbon (PyC) undergoes shrinkage-swelling-amorphization structural evolution under neutron irradiation, leading to significant interface delamination. In hexagonal boron nitride (h-BN), the B element undergoes transmutation (producing He) during neutron exposure, resulting in interfacial layer damage. Similarly, multilayer interfaces composed of PyC and h-BN experience structural disruption under long-term irradiation, which reduces interfacial shear strength and increases frictional stress—making them suboptimal for interface layer applications [1,3].

In recent years, ternary layered MAX phase (a class of nano-laminated materials composed of an early transition-metal (M), an A-group element (A) and C, N, B and/or P (X) [4]) materials have attracted attention as candidates for nuclear-grade interfacial layer [5]. MAX phases have a hexagonal layered crystal structure similar to PyC and h-BN. Under applied stress, they exhibit deformation

 doi:10.20944/preprints202505.2322.v1

characteristics such as slip, buckling, and kinking, which can deflect interfacial cracks and enhance the toughness of composite materials [6]. Additionally, MAX phase materials possess high thermal conductivity, corrosion resistance and radiation resistance [7–11]. As interfacial materials, they contribute positively to both the thermal and radiation tolerance of the composites. Tallman et al. conducted a neutron transmutation analysis and found that the specific activity of MAX phases such as Ti_3SiC_2, Ti_3AlC_2, Ti_2AlC after 10, 30, and 60 years of exposure to thermal and fast neutron spectra is comparable to that of SiC and three orders of magnitude lower than that of nickel-based alloys like Alloy 617 [7,11,12]. Despite their excellent radiation resistance, coating MAX phases onto SiC_f remains a technical challenge [13]. Filber-Demut et al. utilized the electrophoretic deposition method to coat SCS-6 type of SiC_f with Ti_3SiC_2 powder. And also demonstrated significant improvements in debonding strength and interfacial friction resistance in ceramic matrix composites [14]. However, electrophoretic deposition is limited to micron-sized Ti_3SiC_2 particles and often fails to achieve uniform coverage, posing a significant challenge for creating homogeneous interfacial layers.

Our working group was the first to developed a simple method for fabricating carbide/MAX phase interfacial layer via an in-situ reaction in a molten salts bath [15]. We further utilized this technique to synthesize MAX phase interfacial layers such as Ti_2AlC and Ti_3SiC_2 on the surfaces of carbon fibers (C_f). And composite materials were then fabricated using the polymer impregnation and pyrolysis process (PIP). After simulated ion irradiation, these composites exhibited good structural stability and had a good irradiation swelling behavior with SiC [16,17].

However, titanium-based MAX phases decompose into TiC at elevated temperatures (~1400 °C) and show poor oxidation resistance above 1200 °C [18]. This decomposition decreases the shear strength of the composite at high temperatures, and necessitates precise temperature control during the subsequent SiC matrix processing. Therefore, it is necessary to develop a high-temperature-stable MAX phase interfacial layer.

According to previous reports, non-transition metal M_2AX compounds containing Sc, Y, and Lu atoms at the M-site are considered to have a stable structure at high temperatures (~1400 °C) [19]. In addition, rare earth elements are known to impart unique properties [18,20,21], such as enhanced irradiation resistance, as observed in aluminum alloys [22] and likely in the in-plane ordered RE-i-MAX phases [23]. Notably, Sc_2SnC shows lower values of elastic constants (i.e., C_{11}, C_{33}, C_{44}, and C_{66}) compared to Ti_2AlC, Ti_3AlC_2, and Ti_3SiC_2, indicating better deformability and processability.

In the present work, we first used the CVD method to coat a PyC layer onto the surface of SiC_f. These carbon-coated fibers were then immersed in a molten salt environment to in-situ synthesize a Sc_2SnC MAX phase interfacial layer. The effects of the PyC layer structure, the sequence of element addition, element diffusion, and precursor composition on the quality of the resulting MAX phase interfacial layer were systematically investigated.

2. Experimental Details

2.1. Materials

Silicon carbide fiber (SiC_f, Cansas-3303) was supplied by Fujian Liya New Material Co. Ltd. and carbon fiber (C_f, 3k, T300) was provided by Toray Co. Ltd., Japan. Scandium powder (Sc, 300 mesh) and Tin powder (Sn, 300 mesh) were sourced from Shanghai Pantian Powder Materials Co. Ltd. Sodium Chloride (NaCl, 99.5%, Aladdin, China) and Potassium Chloride (KCl, 99%, Aladdin, China) were used as the inert salt bath.

2.2. Preparation of the PyC layer

SiC_f tow was first de-sized under vacuum at 600 °C over 2 hours. A series of PyC interphase layers were then deposited using chemical vapor deposition (CVD). The fiber tow was placed inside a graphite sleeve lined with graphite paper for demolding. The assembly was heated in a quartz tube (*Φ*80*2mm*1.8m) to a final pyrolysis temperature of 900-1100 °C at a ramp rate of 5 °C/min using a furnace (*TL1200-1200*, *Boyuntong*, Nanjing, China). After reaching the target temperature, the system

 doi:10.20944/preprints202505.2322.v1

was allowed to cool naturally to room temperature under vacuum. The base vacuum inside the furnace tube was maintained below 1 Pa before deposition. During the deposition, stable airflow was introduced into the graphite sleeve. Methane (CH_4) and acetylene (C_2H_2) were used as carbon sources, while argon (Ar) served as both a dilution and carrier gas. The structure of the PyC interphase layer was controlled by adjusting CVD parameters, including temperature, residence time, and flow-field-related factors. The flow field is regulated using an automated gas supply system, controlling pressure, gas flux, and precursor composition. The PyC content in the in-situ reaction was estimated based on its layer thickness. The final sample was designated as SiC_f/PyC.

2.3. In-Situ Synthesis of Sc_2SnC Coating

The Sc_2SnC coating was synthesized through the reaction between carbon, scandium powder and tin powder in a molten salt environment. NaCl-KCl eutectic salt (melting point of ~ 660 °C) was used as the inert salt bath. The powders were mixed in a stoichiometric ratio of Sc : Sn = 2 : 1.1 (mol), unless otherwise specified. The tin content was increased to compensate for possible weight loss at high temperatures, as tin has a relatively low melting point, similar to the preparation of Sc_2SnC MAX phase. The starting powders of Sc and Sn were combined with the NaCl-KCl salt in a molar ratio of (Sc + Sn) : (NaCl-KCl) = 1 : 20, and thoroughly ground in an agate mortar. The as-prepared SiC_f/PyC or C_f was placed in the alumina crucible and covered with the mixed powder. The crucible was then placed in a tubular furnace (*SGL-1700, SIOMM*, Shanghai, China) and heated at a rate of 5 °C/min under argon atmosphere. A range of temperatures and dwell times were tested to evaluate their effects on the composition and thickness of the interface layer. After the reaction, the sample was thoroughly washed, filtered and dried at 40 °C under vacuum to remove the inert salt.

2.4. Characterization

The microstructure of the samples was examined by a field-emission scanning electron microscope (*SEM, HITACHI Regulus 8230*, Japan) equipped with an energy-dispersive spectroscopy (*EDS, Detector6, Bruker XFlash*, Germany) system. X-ray diffraction (*XRD*) analysis was performed using an X-ray diffractometer (*Bruker ADVANCE D8*, Germany) using Cu-K_α radiation at a scan rate of 0.02°/s. Raman spectra were obtained using a confocal Raman spectrometer (*HORIBA LabRAM HR Evolution*, Japan) with a 532 nm excitation wavelength.

3. Results

3.1. PyC Pre-Film Synthesis and Characterization

The microstructure of the as-produced PyC influences the structure of Sc_2SnC prepared by the molten salt method. To obtain a uniform and smooth carbon layer, we investigated the structural variations of PyC on SiC_f under different preparation conditions. The temperature range (900 °C, 1000 °C, 1100 °C) was selected based on a comprehensive consideration of the pyrolysis temperature range of acetylene and methane, as well as the impact of temperature on SiC_f. Temperatures exceeding 1200 °C can damage the carbonized fibers [24–28]. Figure 1 shows the morphology and Raman spectra of PyC prepared at different temperatures. The surface morphology reveals that the PyC coating uniformly conforms to SiC_f, forming an intact, dense and smooth layer (Figure 1(a-1)~(c-1)). Upon magnification, some abnormally large particles or granules are visible (indicated by white arrows in Figure 1(b-2),(c-2)), which may be related to the rapid pyrolysis of acetylene, as discussed in Figure 2. Additionally, from the cross-sectional morphology, it is evident that as temperature increases, the PyC layer becomes denser, and the laminar texture becomes more pronounced. Within the temperature range of 900~1100 °C, no noticeable gaps are observed at the interface between the PyC and SiC_f, indicating a strong interfacial bond between the coating and the fibers. The Raman spectra at different temperatures are shown in the Figure 1(a-4)~(c-4). Due to the disordered nature of carbon materials, PyC tend to exhibit similar Raman spectra despite having considerable structural differences [29–31]. To investigate the influence of temperature, spectral deconvolution using five

 doi:10.20944/preprints202505.2322.v1

Raman bands – D_1, G, D_2, D_3 and D_4 – was performed to qualitatively assess the defect levels in the PyC layer through the I_D/I_G ratio [32,33]. Higher temperature results in a lower I_D/I_G ratio (from 3.86 to 2.89, compared to 3.70 for de-sized C_f T300), indicating that the PyC coating is more compact and has fewer defects. Figure 2 shows the microstructural morphology of the PyC coatings prepared with different ratios of CH_4 and C_2H_2. It can be observed that as the C_2H_2 concentration increases, larger particles appear on the surface. This may be due to the higher carbon deposition rate of C_2H_2, which results in insufficient time for carbon atoms to diffuse, leading to local aggregation. From the cross-sectional morphology, it can be seen that when the CH_4-C_2H_2 ratio is 90:60, the resulting PyC coating has a high density and a strong bond with the SiC_f. Additionally, from the Raman spectra, its I_D/I_G ratio is relatively lower, indicating that the PyC has a more compact structure (Figure 2(b)). Given the strict requirements for interface layer thickness, an overly thick layer may lead to interface delamination or stress concentration, while an excessively thin layer may fail to prevent crack propagation. Therefore, precise control of the PyC thickness is crucial. Figure 3 shows the relationship between the PyC thickness (T) and time (t) at 1000 °C with a CH_4-C_2H_2 ratio of 90:60. The statistical data is fitted to a logistic function (1), and it is clear that PyC thickness and deposition time show a nonlinear relationship. This could be attribute to the changes in the adsorption and pyrolysis rates of methane and acetylene gases over time.

$$T = 513.14 - \frac{522.10}{1 + \frac{t^{1.95}}{2069.50}} \quad (1)$$

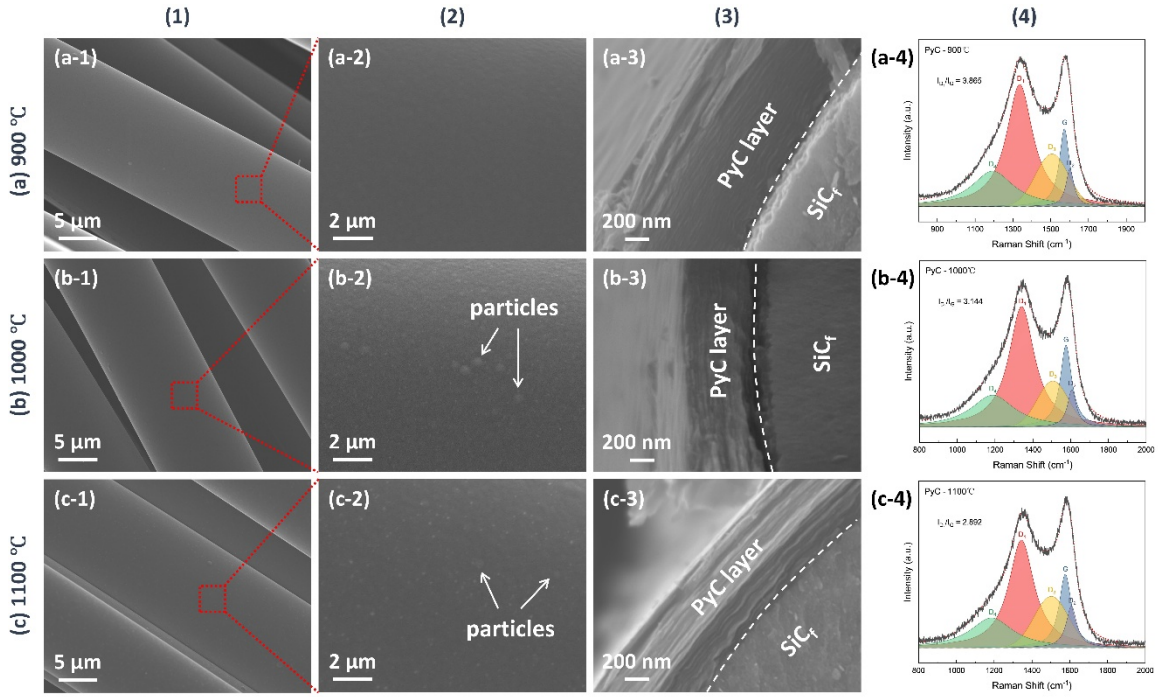

Figure 1. The morphology of PyC pre-film produced at (a) 900 °C, (b) 1000 °C, and (c) 1100 °C, for 60 minutes under 50 kPa in a CH_4-C_2H_2-Ar atmosphere (CH_4 : C_2H_2 : Ar = 90 : 60 : 200 sccm). (1) and (2) shows the surface morphology of the PyC film, with (2) being a magnified view of a selected area in (1), (3) displays the cross-sectional morphology, and (4) presents the corresponding Raman spectra.

Preprints.org (www.preprints.org) | NOT PEER-REVIEWED | Posted: 29 May 2025 doi:10.20944/preprints202505.2322.v1

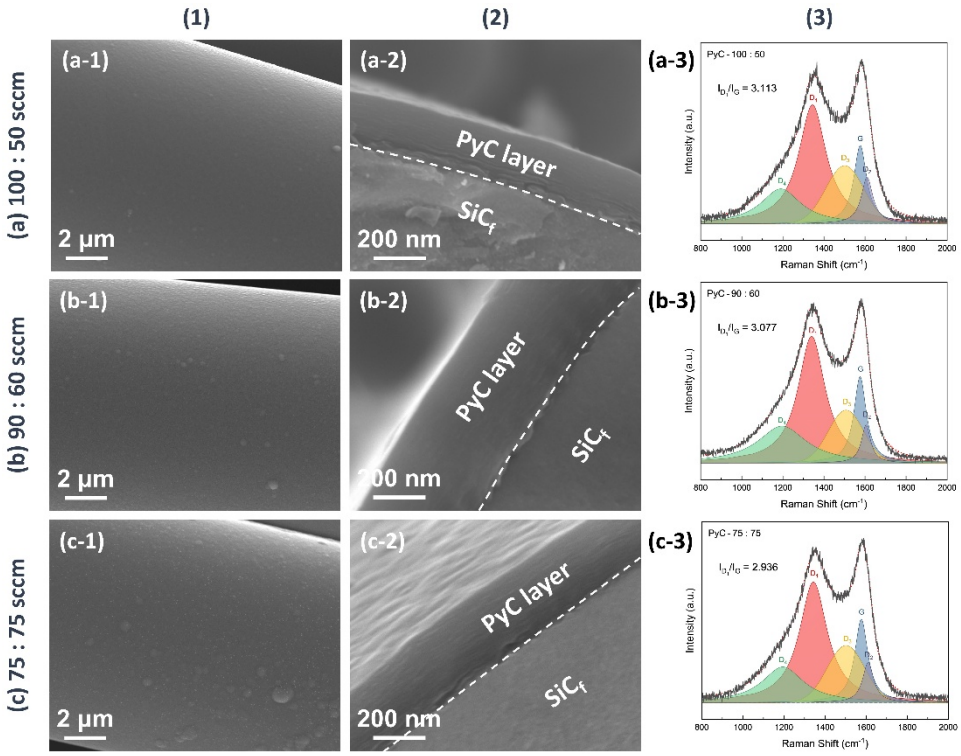

Figure 2. The morphology and Raman spectra of the PyC pre-film produced under different CH_4 and C_2H_2 gas flow ratio - (a) 100 : 50 sccm, (a) 90 : 60 sccm, (a) 75 : 75 sccm - at 1000 °C and 50 kPa. (1) shows the surface morphology, (2) the cross-sectional morphology, and (3) the corresponding Raman spectra. The flow rate of the diluting gas (Ar) is fixed at 200 sccm.

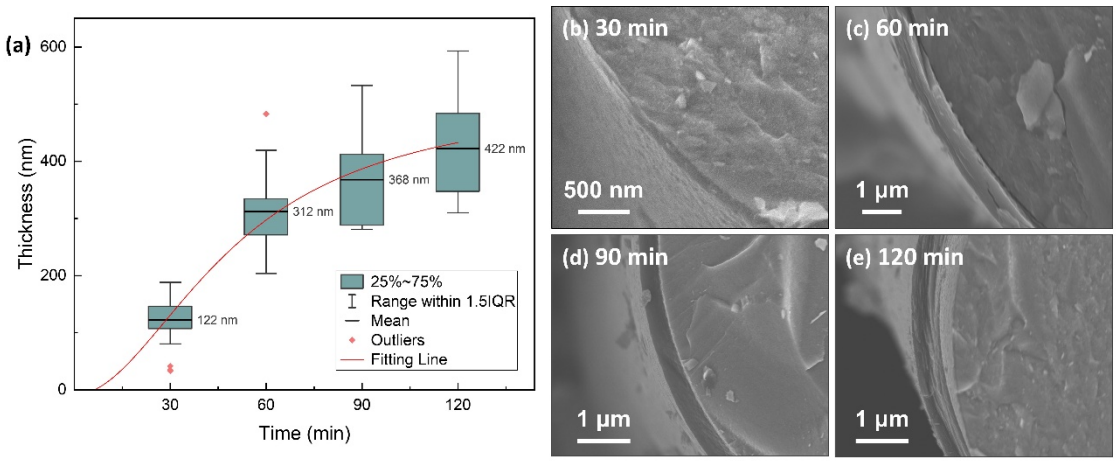

Figure 3. (a) Relationship between time and thickness of PyC pre-film. Typical samples deposited for (b) 30 minutes, (c) 60 minutes, (d) 90 minutes, and (e) 120 minutes are shown on the right.

Table 1. Fitting details of the logistic function for the data in Figure 3(a).

Equation	$T = A_2 + \frac{A_1 - A_2}{1 + (\frac{t}{t_0})^P}$
A_1	- 8.957 ± 76.068

 doi:10.20944/preprints202505.2322.v1

A_2	**513.14 ± 77.330**
t_0	**50.17 ± 9.965**
p	**1.954 ± 0.656**
R-Square	**0.73704**

3.2. MAX Phase Coating

3.2.1. Carbon Fiber Coating (C_f/ScC_x/Sc_2SnC)

The reaction kinetics in the molten salt synthesis of MAX phases vary depending on the carbon structure. To explore an optimal preparation process, we used C_f as a substitute for PyC coatings. This choice was based on the similarity in the amorphous structures and defect levels of C_f and PyC. Furthermore, C_f is more readily available and allows for better control of single variables. Building on our previous work on synthesizing carbon-containing MAX phases at low temperatures using the molten salt method [34–37], we adopted two different synthesis routes for MAX phase coatings using C_f:

1. Direct Molten Salt Route: Sc, Sn, and C_f were directly mixed to form Sc_2SnC.
2. Two-Step Molten Salt Route: Sc and C_f were first mixed to form an intermediate phase, ScC, followed by the introduction of Sn to synthesize Sc_2SnC.

In both routes, the reactions were conducted at 1000 °C for 3 hours, with a Sc-to-C_f molar ratio of 1:1. The XRD patterns of Sc_2SnC synthesized via these two routes are shown in Figure 4. It is evident that neither approach resulted in the significant formation of Sc_2SnC. In the direct molten salt route (Route 1), the primary phase formed was ScC (*Fm*$\bar{3}$*m*, PDF#97-004-3524), with only trace amounts of Sc_2SnC (*P*6_3/*mmc*, Ref. [19]). In the two-step route (Route 2), the intermediate phase ScC was successfully synthesized first; however, after introducing Sn, Sc_2SnC was still not observed. Instead, small amounts of Sc_2O_3 and Sc_2OC were detected, possibly due to oxidation interference. Raman spectroscopy analysis, as shown in Figure 4(b), further supports these findings. In Route 1, three characteristic peaks were observed at 139, 207, and 217 cm^{-1}, corresponding to the ω_1, ω_2, and ω_3 vibrational modes of the 211-type MAX phase. In contrast, Route 2 exhibited only the ω_3 peak, with no other distinct features [38–41]. Notably, the ω_4 vibrational mode at approximately 380 cm^{-1} was not clearly detected. Additionally, peaks observed in the 380-800 cm^{-1} range correspond to carbide materials [42,43], suggesting that the broadening of the ScC peaks in the XRD spectrum may be attributed to non-stoichiometric scandium carbide or ScC_x with a high defect density.

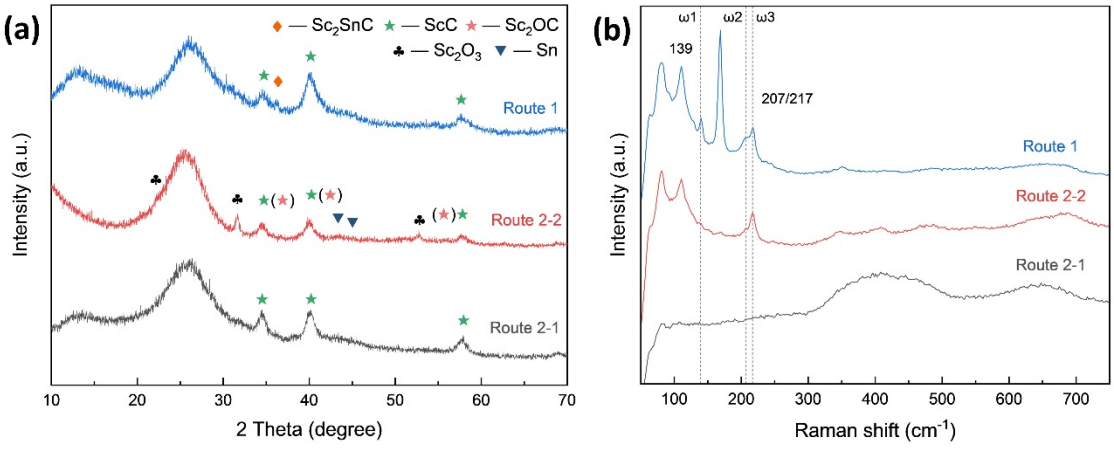

 doi:10.20944/preprints202505.2322.v1

Figure 4. (a) XRD pattern and (b) Raman spectra of C_f reacted in Route 1 and Route 2.

Figure 5 further presents the SEM morphology of the Sc_2SnC coatings synthesized via the two routes. In Route 1, a uniform ultra-thin coating composed of nanocrystals was formed. In Route 2-1, ScC_x exhibited a well-defined coating morphology on the fiber surface, accompanied by a small number of particles. Following the introduction of Sc and Sn, a significant number of nanocrystals appeared on the surface, identified as granular Sc_2O_3 and nano-platelet-like Sc_2SnC. Additionally, partial oxidation led to the formation of accordion-like Sc_2OC or complete oxidation into Sc_2O_3, causing the ScC_x layer to peel off, as indicated by the white arrows in Figure 5(c-1). Consequently, in Route 2-2, oxidation resulted in the loss of Sc, which restricted the reaction process. Given the low conversion rate of Sc_2SnC, it is likely that element diffusion and reaction kinetics are the key controlling factors, which will be further discussed. Based on this analysis, the direct synthesis method (Route 1) is more favorable for the fabrication of Sc_2SnC coatings.

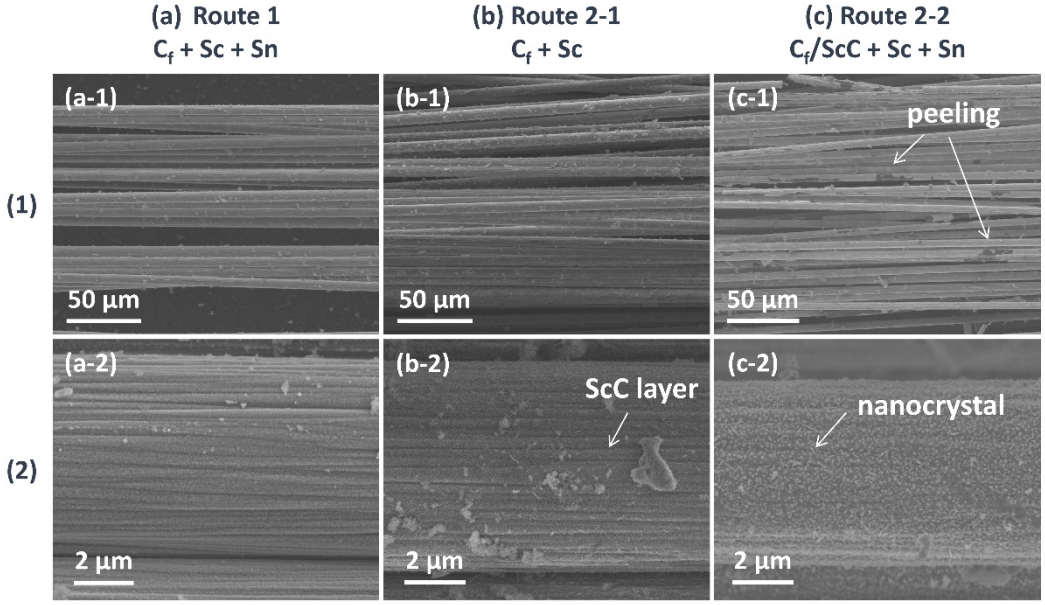

Figure 5. The (1) overview and (2) detailed surface morphology of C_f after (a) Route 1, (b) first step of Route 2, (c) second step of Route 2.

As the Sc_2SnC synthesized by the direct method shows only faint diffraction peaks in Figure 4(a), the reaction appears incomplete under relatively stoichiometric ratio, likely due to insufficient diffusion time. To address this, we extended the reaction duration. As shown in Figure 6, prolonging the reaction time significantly increased the content of both Sc_2SnC and ScC_x, with peak concentrations reached after 4 hours of reaction. However, with further extension, partial transformation of ScC_x occurred due to its metastable nature and tendency to oxidize. Specifically, ScC_x either oxidized to form Sc_2OC ($Fm\bar{3}m$, PDF#97-015-6683) or was reduced to Sc_3C_4 ($P4/mnc$, PDF#97-007-1145). As the fibers were held at high temperature for a longer period, the transformation to Sc_2OC continued, while the formation of Sc_3C_4 was limited due to the restricted diffusion of carbon. Both transformation pathways are accompanied by lattice expansion, which can induce stress or even cause cracking. Overall, excessive reaction time can damage the fibers, leading to coating delamination or pulverization.

 doi:10.20944/preprints202505.2322.v1

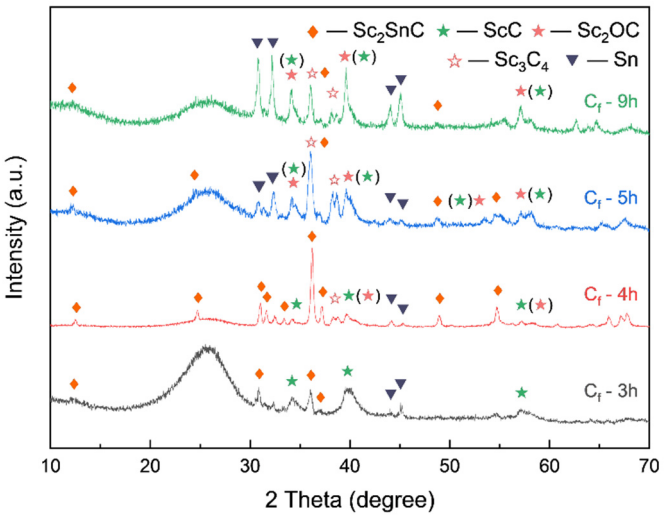

Figure 6. XRD pattern of C_f after long term dwelling in molten salt.

Figure 7 presents the microstructural morphology of Sc_2SnC coatings formed at different reaction durations. At 3 hours, the Sc_2SnC appears as isolated hexagonal sheets that seem to be "embedded" within C_f. This unique morphology resembles the loading of nanocrystals rather than a uniform coating, which is confirmed by mapping in Figure 8. As the reaction proceeds, the Sc_2SnC sheets gradually accumulate and form a dense coating through a radial growth mode. After 4 hours of treatment (as shown in Figure 7(b)), the material exhibits a well-defined crystalline structure. Interestingly, as the reaction continues, these distinctive crystals grow independently, reaching a maximum size of approximately 5 μm. Correspondingly, the thickness of the Sc_2SnC coating increases to around 50 nm, 500 nm, and 2.9 μm after 3, 4, and 5 hours of reaction, respectively. A scandium carbide (ScC_x) layer is observed only in the 5-hour samples. It forms a dense interfacial layer between the Sc_2SnC coating and the C_f substrate, and its thickness increases along with the Sc_2SnC layer. Although it is challenging to distinguish ScC_x from Sc_2OC and Sc_3C_4 using SEM imaging and elemental mapping, these by-products possess larger lattice parameters and introduce residual stress within the coating. The stress may ultimately lead to the formation of cracks, a phenomenon that already observed in the 4-hour sample.

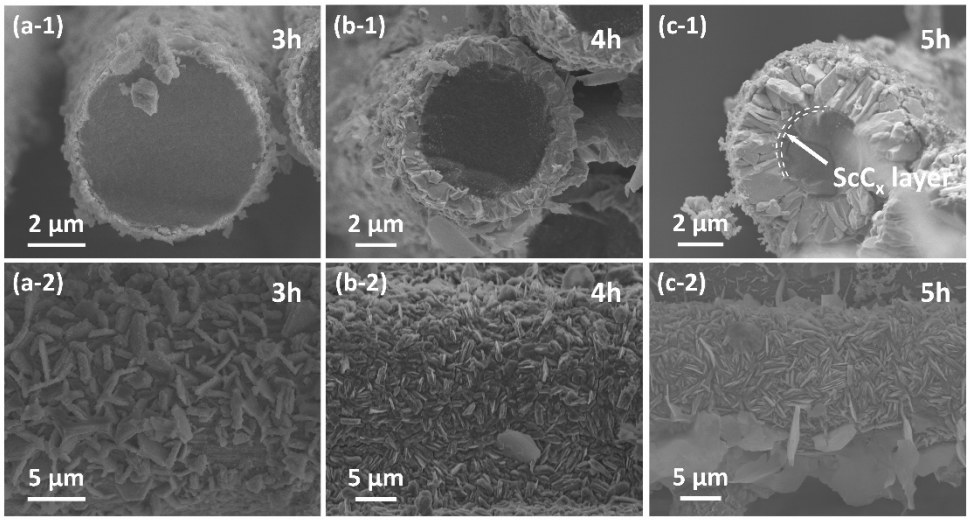

Figure 7. The cross-sectional and surface morphology evolution of C_f after (a) 3h, (b) 4h and (c) 5h reaction.

 doi:10.20944/preprints202505.2322.v1

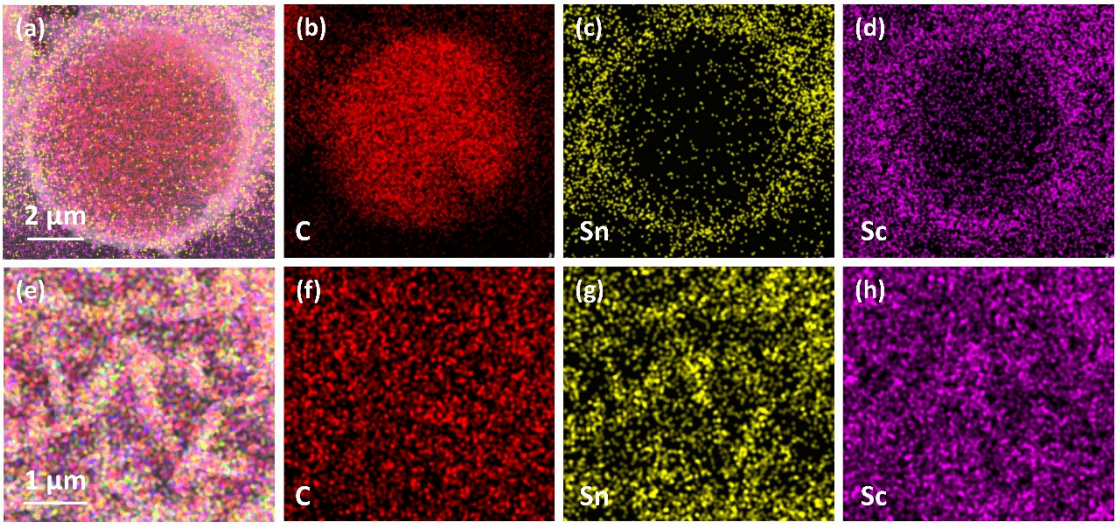

Figure 8. The mapping results of (a-d) cross section, (e-h) surface of C_f-3h sample.

According to the growth mechanism of molten salt synthesis for MAX phases, the general reaction equations (2-4) are listed in order of increasing temperature. Eutectic salts create an ionized environment at relatively low temperatures, facilitating the formation of Sc-Sn intermetallic compounds and ScC_x. ScC_x is considered the most critical intermediate product in the reaction. Due to the high melting points of both scandium and carbon, the carbide layer can only form at around 1000 °C, primarily at reaction interfaces characterized by abundant defects and preferred crystallographic orientations. Once ScC_x is formed, the reaction between the Sc-Sn intermetallic compound and scandium carbide can proceed. With the assistance of molten salts, elemental species are rapidly transported to the reaction interface. Meanwhile, the abundant defects in the non-stoichiometric ScC_x provide pathways for the diffusion of Sc and Sn. As a result, Sc_2SnC exhibits a high nucleation and growth rate, which explains the absence of a distinct ScC_x layer during the early stages of the reaction. Furthermore, the presence of multiple close-packed crystal planes and a high c/a ratio leads to anisotropic growth behavior in Sc_2SnC, typically resulting in flake-like structures.

$$Sc + Sn \leftrightarrow Sc\text{-}Sn\ (intermetallic) \quad (2)$$

$$Sc + C \xrightarrow{molten\ chloride} ScC_x \quad (3)$$

$$ScC_x + Sc\text{-}Sn \xrightarrow{molten\ chloride} Sc_2SnC \quad (4)$$

The reaction follows a template synthesis mechanism in which Sc_2SnC inherits the structure of its precursors — from the graphite-like PyC layer to the cubic ScC phase. Specifically, under suitable conditions, Sc_2SnC nucleates and grows along the [111] plane or its equivalent planes, such as $[1\bar{1}\bar{1}]$, which is rotated 75.53° from [111] plane of cubic crystal. This growth is typically aligned parallel or nearly perpendicular to the fiber axis. In addition, the slight preferred orientation of ScC in the {200} plane provides numerous nucleation sites along the {111} family of planes. As a result, Sc_2SnC flakes initially grow nearly perpendicular to the surface of the C_f. Once a continuous and dense Sc_2SnC coating is formed, the diffusion channels are largely closed. At this point, the metastable ScC phase (with a formation enthalpy of ΔH_{form} = – 0.138 eV, according to the Materials Project) may transform into the thermodynamically stable Sc_3C_4 phase (ΔH_{form} = –0.408 eV) via carbon diffusion. This transformation could lead to structural pulverization and delamination. Ultimately, a multilayered interface consisting of ScC_x and Sc_2SnC is formed on the surface of C_f.

 doi:10.20944/preprints202505.2322.v1

3.2.2. Silicon Carbide Fiber Coating (SiC_f/ScC_x/Sc_2SnC)

Based on the growth mechanism observed on C_f, the reaction was transferred onto SiC_f substrates coated with an approximately 370 nm PyC layer. The synthesis was performed at 1000 °C for 3 hours, using varying Sc : Sn molar ratios. Figure 9(a) presents the XRD patterns of all SiC_f coatings. As the reaction progresses, the amorphous peak gradually diminishes, while the characteristic diffraction peaks of Sc_2SnC and ScC_x/Sc_2OC start to appear. Notably, the Sc_3C_4 phase is only observed in the sample with a 3:2 ratio (SiC_f/Sc_2SnC-3:2). The composition of the interface is further confirmed by the Raman spectra shown in Figure 9(b). Four distinct peaks at 139, 207, 217, and 380 cm^{-1} correspond to the typical vibrational modes of the 211-type MAX phase. Among these, the peaks at 207 and 380 cm^{-1} show significant enhancement, indicating structural differences in the coating, even though the XRD patterns remain relatively unchanged. Additionally, a previously unreported peak appears around 320 cm^{-1}, for which no known vibrational mode has been identified. Some studies have observed similar satellite peaks in 211 MAX phases, although they have not been extensively studied. As expected, Sc_2SnC coatings formed under different Sc : Sn ratios exhibit three distinct morphologies. Under the stoichiometric condition (Sc : Sn = 2 : 1), Sc_2SnC displays the same flake-like morphology as seen on C_f substrates, as shown in Figure 10(a). The elemental mapping of the scaly surface is presented in Figure 11(h-l). The cross-sectional image reveals that a significant amount of PyC remains unreacted.

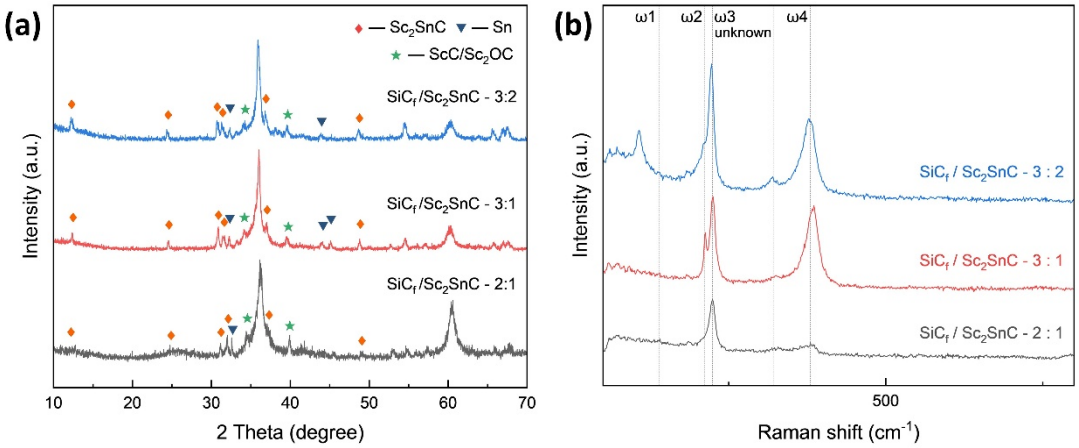

Figure 9. (a) XRD pattern and (b) Raman spectra of SiC_f with PyC layer reacted within different ingredient ratio, the samples are named after SiC_f/Sc_2SnC - (Sc : Sn ratio).

 doi:10.20944/preprints202505.2322.v1

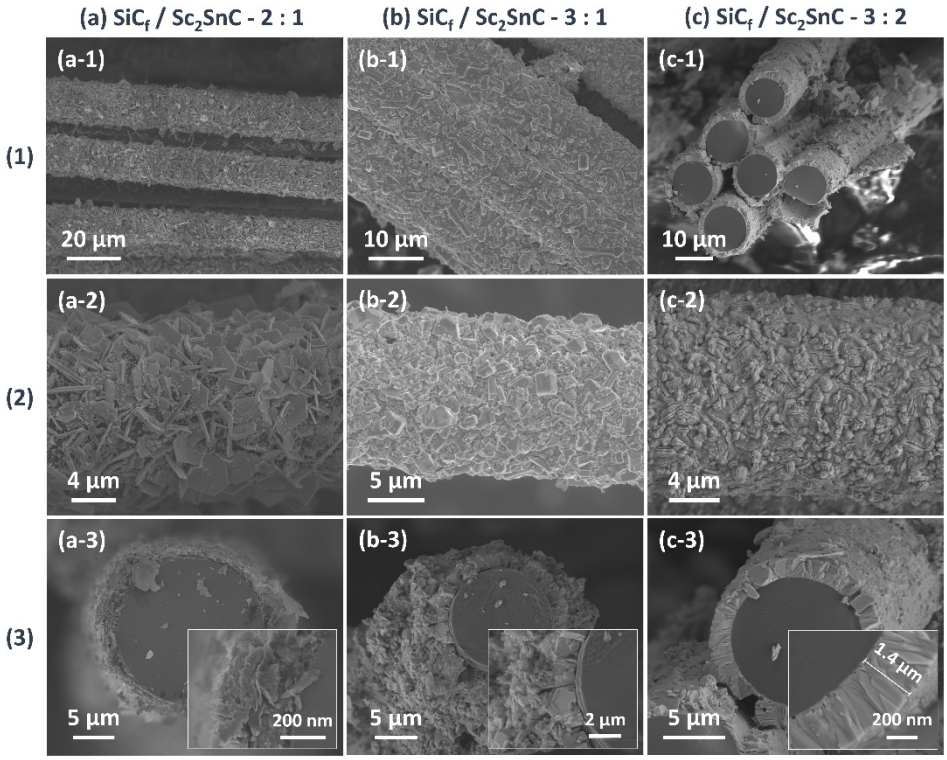

Figure 10. The morphology of Sc_2SnC coating produced within different ingredient ratio at 1000 ℃ for 3h. (1) Overview, (2) surface and (3) cross-section images. (a) SiC_f/Sc_2SnC - 2:1, (b) SiC_f/Sc_2SnC - 3:1 and (c) SiC_f/Sc_2SnC - 3:2.

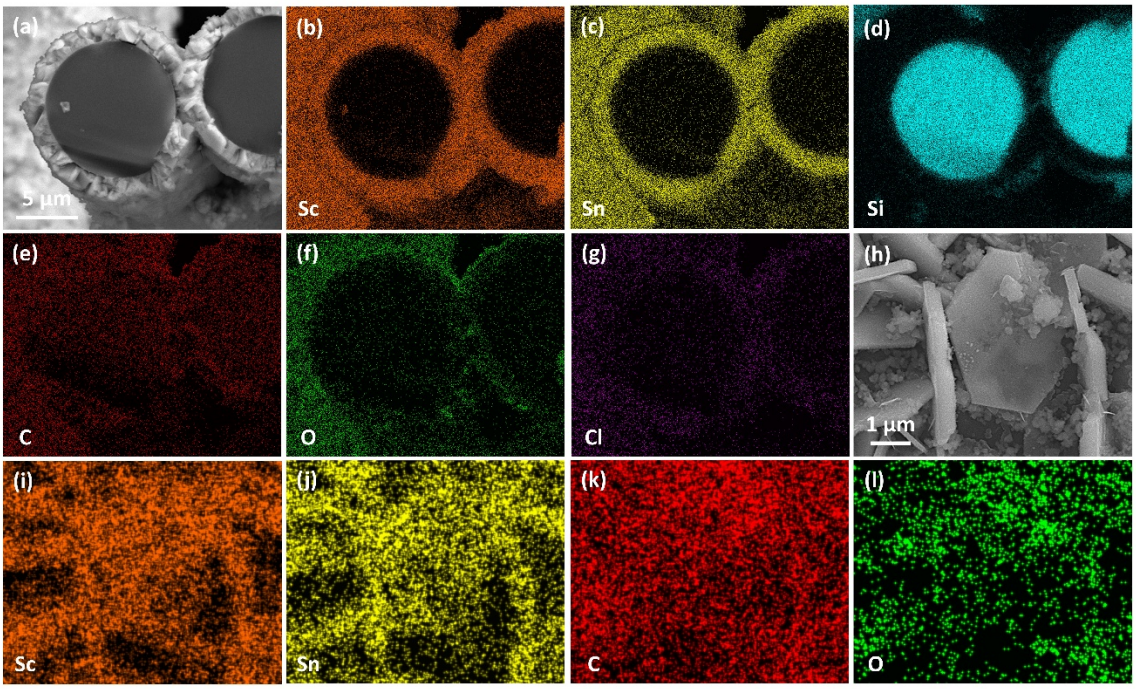

Figure 11. Elemental mapping of Sc_2SnC coatings on SiC_f. (a–g) Cross-sectional elemental distribution of the SiC_f/Sc_2SnC-3:2. (h–l) Surface elemental distribution of the SiC_f/Sc_2SnC-2:1.

When the Sc : Sn atomic ratio is increased to 3:1, the resulting coating becomes dense and continuous, consisting of nanocrystalline structures. Notably, some surface particles exhibit abnormal grain growth, forming equiaxed crystals with diameters up to 1.8 µm. However, this rapid

 doi:10.20944/preprints202505.2322.v1

grain growth leads to structural inhomogeneity and localized pulverization. In cross-sectional observations, the Sc_2SnC layer shows weak adhesion to the unreacted PyC layer, likely due to residual stresses arising from mismatched thermal expansion coefficients.

At a Sc:Sn ratio of 3:2, a more uniform and finer Sc_2SnC coating is formed, with a thickness of approximately 1.4 μm. No delamination is observed between the coating and the SiC_f substrate. The measured thickness is consistent with the theoretical lattice expansion from PyC (a = 0.247 nm, c = 0.693 nm; graphite, PDF#97-061-7290) to Sc_2SnC (a = 0.337 nm, c = 1.464 nm, Ref. [19]), indicating the complete transformation of PyC. This coating exhibits excellent uniformity and strong interfacial adhesion, with surface cracks attributed only to the formation of by-products.

Cross-sectional elemental mapping (Figure 11(a–g)) confirms the uniform distribution of scandium and tin within the coating, as well as the structural integrity of the SiC_f substrate. In addition, the high oxygen concentration detected on the surface is likely due to the formation of Sc_2OC and the adsorption of atmospheric oxygen.

4. Conclusions

(1) A dense and uniformly coated PyC layer was successfully deposited on SiC_f via CVD by precisely controlling the reaction temperature at 1000 °C and setting the CH_4:C_2H_2 gas ratio to 90:60.

(2) ScC_x/Sc_2SnC composite coatings were synthesized on the surfaces of C_f and SiC_f using a molten salt method. In the early stages of the reaction, isolated hexagonal Sc_2SnC flakes nucleated and grew on the C_f surface. With extended reaction time, these nearly vertically oriented flakes gradually accumulated to form a continuous coating, with the thickness progressively increasing from 50 nm to 500 nm and ultimately to 2.9 μm.

(3) During the reaction process, the formation of ScC_x exhibited sluggish kinetics, making it a key intermediate that governed the overall reaction pathway. The high defect density and preferential orientation observed in ScC_x contributed to the distinctive microstructure and growth direction of the resulting Sc_2SnC phase. Raman spectroscopy confirmed the presence of both ScC_x and Sc_2SnC. However, due to its metastable nature, ScC_x is prone to phase transformation into Sc_2OC and Sc_3C_4, which may lead to cracking, pulverization, interfacial debonding, and eventual delamination of the coating—a challenge that remains difficult to mitigate.

Acknowledgments: his study was supported financially by the National Natural Science Foundation of China (grant no. 12435017) and the Ningbo Top-talent Team Program. Q. H. acknowledges support by Ten-Thousand Talents Plan of Zhejiang Province (grant no. 2022R51007).

References

1. KATOH Y, OZAWA K, SHIH C, NOZAWA T, SHINAVSKI R J, HASEGAWA A, SNEAD L L. Continuous SiC fiber, CVI SiC matrix composites for nuclear applications: Properties and irradiation effects [J]. Journal of Nuclear Materials, 2014, 448(1): 448-476, 10.1016/j.jnucmat.2013.06.040.
2. NASLAIN R, PAILLER R, LAMON J. Single- and Multi-Layered Interphases in SiC/SiC Composites Exposed to Severe Conditions: An Overview [M]. Ceramics in Nuclear Applications. 2009: 1-18, 10.1002/9780470584002.ch1.
3. OUYANG Q, WANG Y F, XU J, LI Y S, PEI X L, MO G M, LI M A, LI P, ZHOU X B, GE F F, et al. Research Progress of SiC Fiber Reinforced SiC Composites for Nuclear Application [J]. Journal of Inorganic Materials, 2022, 37(8): 821-840, 10.15541/jim20220145.
4. DAHLQVIST M, BARSOUM M W, ROSEN J. MAX phases – Past, present, and future [J]. Materials Today, 2024, 72: 1-24, 10.1016/j.mattod.2023.11.010.
5. DANG X, FAN X, YIN X, MA Y, MA X. Research Progress on Multi-functional Integration MAX Phases Modified Continuous Fiber-reinforced Ceramic Matrix Composites [J]. Journal of Inorganic Materials, 2020, 35(1): 29-34, 10.15541/jim20190400.

 doi:10.20944/preprints202505.2322.v1

6. GONZALEZ-JULIAN J. Processing of MAX phases: From synthesis to applications [J]. Journal of the American Ceramic Society, 2021, 104(2): 659-690, 10.1111/jace.17544.
7. TALLMAN D J, HOFFMAN E N, CASPI E A N, GARCIA-DIAZ B L, KOHSE G, SINDELAR R L, BARSOUM M W. Effect of neutron irradiation on select MAX phases [J]. Acta Materialia, 2015, 85: 132-143, 10.1016/j.actamat.2014.10.068.
8. MAGNUS C, COOPER D, JANTZEN C, LAMBERT H, ABRAM T, RAINFORTH M. Synthesis and high temperature corrosion behaviour of nearly monolithic Ti_3AlC_2 MAX phase in molten chloride salt [J]. Corrosion Science, 2021, 182: 109193, 10.1016/j.corsci.2020.109193.
9. ANG C, SILVA C, SHIH C, KOYANAGI T, KATOH Y, ZINKLE S J. Anisotropic swelling and microcracking of neutron irradiated Ti_3AlC_2–$Ti_5Al_2C_3$ materials [J]. Scripta Materialia, 2016, 114: 74-78, 10.1016/j.scriptamat.2015.11.008.
10. WANG C, YANG T, TRACY C L, LU C, ZHANG H, HU Y-J, WANG L, QI L, GU L, HUANG Q, et al. Disorder in $M_{n+1}AX_n$ phases at the atomic scale [J]. Nature Communications, 2019, 10(1): 622, 10.1038/s41467-019-08588-1.
11. WANG J, SHU R, DONG Y, SHAO T, DENG Q H, ZHOU X B, HUANG F, DU S Y, WANG Z G, XUE J M, et al. Microstructure evolution of V_2AlC coating on Zr substrate under He irradiation and their mechanical behavior [J]. Scripta Materialia, 2017, 137: 13-17, 10.1016/j.scriptamat.2017.05.003.
12. TALLMAN D J, HE L, GARCIA-DIAZ B L, HOFFMAN E N, KOHSE G, SINDELAR R L, BARSOUM M W. Effect of neutron irradiation on defect evolution in Ti_3SiC_2 and Ti_2AlC [J]. Journal of Nuclear Materials, 2016, 468: 194-206, 10.1016/j.jnucmat.2015.10.030.
13. LI M, ZHOU X, YANG H, DU S, HUANG Q. The critical issues of SiC materials for future nuclear systems [J]. Scripta Materialia, 2018, 143: 149-153, 10.1016/j.scriptamat.2017.03.001.
14. FILBERT-DEMUT I, BEI G, HöSCHEN T, RIESCH J, TRAVITZKY N, GREIL P. Influence of Ti_3SiC_2 Fiber Coating on Interface and Matrix Cracking in an SiC Fiber-Reinforced Polymer-Derived Ceramic [J]. Advanced Engineering Materials, 2015, 17(8): 1142-1148, 10.1002/adem.201500192.
15. LI M, WANG K, WANG J, LONG D, LIANG Y, HE L, HUANG F, DU S, HUANG Q. Preparation of TiC/Ti_2AlC coating on carbon fiber and investigation of the oxidation resistance properties [J]. Journal of the American Ceramic Society, 2018, 101(11): 5269-5280, 10.1111/jace.15784.
16. WANG K, LI M, LIANG Y, WANG J, HE L, DU S, HUANG Z, HUANG Q. Interface modification of carbon fibers with TiC/Ti_2AlC coating and its effect on the tensile strength [J]. Ceramics International, 2019, 45(4): 4661-4666, 10.1016/j.ceramint.2018.11.156.
17. WANG J, WANG K, PEI X, LI M, YUAN Q, ZHU Y, YANG Y, ZHANG C, HE L, DU S, et al. Irradiation behavior of C_f/SiC composite with titanium carbide (TiC)-based interphase [J]. Journal of Nuclear Materials, 2019, 523: 10-15, 10.1016/j.jnucmat.2019.05.043.
18. BARSOUM M W. The MN+1AXN phases: A new class of solids: Thermodynamically stable nanolaminates [J]. Progress in Solid State Chemistry, 2000, 28(1): 201-281, 10.1016/S0079-6786(00)00006-6.
19. LI Y B, QIN Y Q, CHEN K, CHEN L, ZHANG X, DING H M, LI M A, ZHANG Y M, DU S Y, CHAI Z F, et al. Molten Salt Synthesis of Nanolaminated Sc_2SnC MAX Phase [J]. Journal of Inorganic Materials, 2021, 36(7): 773-778, 10.15541/jim20200529.
20. EKLUND P, BECKERS M, JANSSON U, HöGBERG H, HULTMAN L. The $M_{n+1}AX_n$ phases: Materials science and thin-film processing [J]. Thin Solid Films, 2010, 518(8): 1851-1878, 10.1016/j.tsf.2009.07.184.
21. CHOWDHURY A, ALI M A, HOSSAIN M M, UDDIN M M, NAQIB S H, ISLAM A K M A. Predicted MAX Phase Sc_2InC: Dynamical Stability, Vibrational and Optical Properties [J]. physica status solidi (b), 2018, 255(3): 1700235, 10.1002/pssb.201700235.
22. IVANOV L I, IVANOV V V, LAZORENKO V M, PLATOV Y M, TOVTIN V I, TOROPOVA L S. Radiation resistance and parameters of activation of aluminium-magnesium-scandium and aluminium-magnesium-vanadium alloys under neutron irradiation [J]. Journal of Nuclear Materials, 1992, 191-194: 1075-1079, 10.1016/0022-3115(92)90640-7.
23. WANG C, TRACY C L, EWING R C. Radiation effects in $M_{n+1}AX_n$ phases [J]. Applied Physics Reviews, 2020, 7(4), 10.1063/5.0019284.

 doi:10.20944/preprints202505.2322.v1

24. XIAO Y, MA C, XU H, LI G, LIU C, ZHENG R, LI L. Mechanical properties and microstructural evolution of Cansas-III SiC fibers after thermal exposure in different atmospheres [J]. Ceramics International, 2022, 48(22): 32804-32816, 10.1016/j.ceramint.2022.07.206.
25. MA Y, MENG X, CUI Y, KOU S, YANG S, GUO C, DENG J, FAN S. Effect of heat treatment on interface failure behavior in SiC_f/PyC/SiC composites reinforced with Cansas-3 fibers [J]. Ceramics International, 2024, 50(16): 28102-28112, 10.1016/j.ceramint.2024.05.108.
26. WANG P, LIU F, WANG H, LI H, GOU Y. A review of third generation SiC fibers and SiC_f/SiC composites [J]. Journal of Materials Science & Technology, 2019, 35(12): 2743-2750, 10.1016/j.jmst.2019.07.020.
27. NAROTTAM P B. Handbook of Ceramic Composites [M]. New York: Springer 2005, 10.1007/b104068.
28. BERNARD S, CORNU D, MIELE P, WEINMANN M, ALDINGER F. Polyborosilazane-Derived Ceramic Fibers in the Si-B-C-N Quaternary System for High-Temperature Applications [M]. Mechanical Properties and Performance of Engineering Ceramics and Composites: Ceramic Engineering and Science Proceedings. 2005: 35-42, 10.1002/9780470291221.ch5.
29. KANIYOOR A, RAMAPRABHU S. A Raman spectroscopic investigation of graphite oxide derived graphene [J]. AIP Advances, 2012, 2(3): 032183, 10.1063/1.4756995.
30. DING J, SHAO H, HU B, LIU D, SHEN L, SHEN Q. Effect of Heat Treatment on the Shear Strength of SiC/PyC/SiC Composites [J]. Journal of Materials Engineering and Performance, 2024, 33(24): 13803-13814, 10.1007/s11665-023-08972-5.
31. YIFAN X, WEIJIE L, ZHONGWEI Z, XU P, YU L. Process Control of PyC Interphases Microstructure and Uniformity in Carbon Fiber Cloth [J]. Journal of Inorganic Materials, 2024, 39(4): 399-408, 10.15541/jim20230512.
32. ALEXANDER R, KAUSHAL A, RAO P T, PRAKASH J, DASGUPTA K. Identification and classification of disordered carbon materials in a composite matrix through machine learning approach integrated with Raman mapping [J]. Diamond and Related Materials, 2024, 142: 110741, 10.1016/j.diamond.2023.110741.
33. SADEZKY A, MUCKENHUBER H, GROTHE H, NIESSNER R, PöSCHL U. Raman microspectroscopy of soot and related carbonaceous materials: Spectral analysis and structural information [J]. Carbon, 2005, 43(8): 1731-1742, 10.1016/j.carbon.2005.02.018.
34. DASH A, VAßEN R, GUILLON O, GONZALEZ-JULIAN J. Molten salt shielded synthesis of oxidation prone materials in air [J]. Nature Materials, 2019, 18(5): 465-470, 10.1038/s41563-019-0328-1.
35. SUN Q, ZHU S, SHEN Z, LIU Y, WU C, KANG L, YANG Y. Molten-salt assisted synthesis of two-dimensional materials and energy storage application [J]. Materials Today Chemistry, 2023, 29: 101419, 10.1016/j.mtchem.2023.101419.
36. LIU X, FECHLER N, ANTONIETTI M. Salt melt synthesis of ceramics, semiconductors and carbon nanostructures [J]. Chemical Society Reviews, 2013, 42(21): 8237-8265, 10.1039/C3CS60159E.
37. LI S, SONG J, CHE Y, JIAO S, HE J, YANG B. Advances in Molten Salt Synthesis of Non-oxide Materials [J]. ENERGY & ENVIRONMENTAL MATERIALS, 2023, 6(2): e12339, 10.1002/eem2.12339.
38. PRESSER V, NAGUIB M, CHAPUT L, TOGO A, HUG G, BARSOUM M W. First-order Raman scattering of the MAX phases: Ti_2AlN, $Ti_2AlC_{0.5}N_{0.5}$, Ti_2AlC, $(Ti_{0.5}V_{0.5})_2AlC$, V_2AlC, Ti_3AlC_2, and Ti_3GeC_2 [J]. Journal of Raman Spectroscopy, 2012, 43(1): 168-172, 10.1002/jrs.3036.
39. SPANIER J E, GUPTA S, AMER M, BARSOUM M W. Vibrational behavior of the $M_{n+1}AX_n$ phases from first-order Raman scattering (M=Ti, V, Cr, A=Si, X=C, N) [J]. Physical Review B, 2005, 71(1): 012103, 10.1103/PhysRevB.71.012103.
40. BENTZEL G W, NAGUIB M, LANE N J, VOGEL S C, PRESSER V, DUBOIS S, LU J, HULTMAN L, BARSOUM M W, CASPI E A N. High-Temperature Neutron Diffraction, Raman Spectroscopy, and First-Principles Calculations of Ti_3SnC_2 and Ti_2SnC [J]. Journal of the American Ceramic Society, 2016, 99(7): 2233-2242, 10.1111/jace.14210.
41. YU J, CUI L, HE H, YAN S, HU Y, WU H. Raman spectra of RE_2O_3 (RE=Eu, Gd, Dy, Ho, Er, Tm, Yb, Lu, Sc and Y): laser-excited luminescence and trace impurity analysis [J]. Journal of Rare Earths, 2014, 32(1): 1-4, 10.1016/S1002-0721(14)60025-9.

 doi:10.20944/preprints202505.2322.v1

42. KALEMOS A, MAVRIDIS A, HARRISON J F. Theoretical Investigation of Scandium Carbide, ScC [J]. The Journal of Physical Chemistry A, 2001, 105(4): 755-759, 10.1021/jp003031p.
43. KLEIN M V, HOLY J A, WILLIAMS W S. Raman scattering induced by carbon vacancies in TiC_x [J]. Physical Review B, 1978, 17(4): 1546-1556, 10.1103/PhysRevB.17.1546.